Yong Wang
School of Chemical & Biomolecular Engineering,
Georgia Institute of Technology,
Atlanta, GA 30332-0100

Guang Yuan

Yong-Kyu Yoon

Mark G. Allen

School of Electrical and Computer Engineering,
Georgia Institute of Technology,
Atlanta, GA 30332-0100

Sue Ann Bidstrup
School of Chemical & Biomolecular Engineering,
Georgia Institute of Technology,
Atlanta, GA 30332-0100

Optimization of Synthetic Jet Fluidic Structures in Printed Wiring Boards

The active cooling substrate in this study is a microelectromechanical system device that implements the synthetic jet concept into a printed wiring board (PWB) to enhance thermal management. Synthetic jets are oscillatory jets synthesized from the surrounding fluid using electromagnetic actuators. The jet fluid mechanics and heat transfer applications have been investigated by a variety of on-board (PWB) fluidic structures. A testbed comprising six different fluidic channels has been fabricated and characterized with a standard silicon based platinum heater. Based on the fluid mechanics measurements and cooling performance tests, an empirical correlation of synthetic jet Nusselt number with its Reynolds number, fluidic channel dimensions, and jet locations has been derived. Through a magnitude analysis, jet actuator diaphragm, fluidic channel dimension, and cooling location optimizations have been investigated. [DOI: 10.1115/1.2351900]

Introduction

Advanced cooling techniques are required for highly integrated microsystems [1]. Thermal management can be enhanced by heat conduction, convection and radiation. Air cooling rather than liquid cooling is still a dominant heat removal approach among the convection technologies because the fabrication process is much simpler and the fluid impact on the device reliability is minimal [2]. This work is focused on increasing the air cooling device efficiency and performance. An approach is proposed to add an active microfluidic structure into a printed wiring board (PWB) to enhance its heat convection. The microfluidic structure is referred to as the active cooling substrate (ACS), which is based on synthetic jet technology. Optimization of the fluidic structures has been investigated.

Active Cooling Substrate Testbed

Synthetic jets are oscillatory jets generated by a vibration source. The jets are composed of entrained ambient fluid and featured by vortices created at the edges of a sharp orifice [3,4]. Figure 1 shows the concept of a synthetic jet comprising rigid side walls, a flexible diaphragm and a rigid cover plate with a small orifice. Vibrations of the diaphragm periodically draw and eject fresh air into and out of the cavity. When the airflow passes through the orifice, vortices are generated near the exit region, which can entrain more air into the jet core and propagate downstream into a turbulent flow. One vibration cycle can be divided into an impingement stroke and an intake stroke. The impingement stroke is the half-cycle in which the air is discharged; the intake stroke is the half-cycle in which the cavity is refilled. Synthetic jets have been widely used for flow control [5,6]. The use of a synthetic jet in a microsystem packaging for thermal management is an emerging application. It can be used in cooling technology because of its unique characteristics, flow entrainment, and vortex structures. Compared with the conventional impingement jets, the high-momentum synthetic jets generated from the actuator result in more ambient air being entrained into jet flow, and hence, better heat transfer. Vortex structures introduce more disturbances as jets propagate, which lead to better mixing and facilitate heat transfer.

The vibration diaphragm is a key component of the ACS device. In this study, the diaphragm is fabricated by a polymeric material, Dyneon™ fluoroelastomer (3M Corporation, St. Paul, MN), and is excited by an electromagnetic driver. Instead of flat membranes, the polymeric diaphragm has specially designed corrugation structures surrounding its rigid center. As indicated in the schematic diagram of Fig. 2, the axis-symmetric triangular shape corrugated rings are built into the thickness of the driving diaphragm. Corrugation structures facilitate the diaphragm to extend its linear deflection region. Optimization of the corrugation structures directly impacts the synthetic jet generation. An optimal diaphragm structure should ensure a large displacement with small energy cost.

Larger diaphragm displacement increases the jet volumetric flow rate, which leads to higher heat dissipation. Based on the diaphragm dimensions, displacement, and frequency, the volumetric flow rate (Q_v) during impingement strokes for synthetic jets under the assumption that air compressibility is ignored (an assumption that is valid when the velocity is significantly less than the velocity of sound)

$$Q_v = \Delta V(2f) = \frac{\pi}{3}(b^2 + ab + a^2)\left(\frac{D}{2}\right)(2f) = \frac{\pi}{3}(b^2 + ab + a^2)Df \tag{1}$$

where ΔV is the volume change during diaphragm vibration from rest position to full impingement position that is approximated as a frustum of a cone, a is the radius of the diaphragm, b is the radius of the diaphragm rigid center, D is the displacement of the diaphragm, and f is the resonance frequency of the diaphragm system.

Although a larger diaphragm is capable to generate stronger jets, it requires more excitement power. In microelectronic applications, low power consumption is a constraint with the diaphragm design. For a corrugated diaphragm, the resistance to a loading force is due to both bending and tensile forces. The bending effect is linearly proportional to the diaphragm displacement. The tensile forces are negligible at low displacement but become more significant at large displacement, because the tensile effect is

Contributed by the Electronic and Photonic Packaging Division of ASME for publication in the JOURNAL OF ELECTRONIC PACKAGING. Manuscript received May 12, 2005; final manuscript received February 20, 2006. Review conducted by Stephen McKeown.

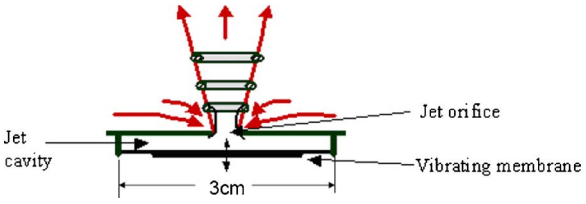

Fig. 1 Schematic of a synthetic jet

proportional to the third order of the diaphragm displacement. Based on the method of superposition, Giovanni [7] related static force with corrugated diaphragm deflection by the following characteristic equation

$$F = \left(\frac{\pi E h^3}{a^2} K_F A_F\right)\left(\frac{D}{2}\right) + \left(\frac{\pi E h}{a^2} L_F B_F\right)\left(\frac{D}{2}\right)^3 \tag{2}$$

where F is the static force applied on the diaphragm, h is the thickness of the corrugation structure, H is the depth of corrugation, and E is the material elasticity modulus. A_F is the flexural force coefficient and B_F is the tension force coefficient, which are functions of the ratio h/H. A_F decreases as h/H increases, while B_F increases as h/H increases. K_F is the bending stiffness coefficient, and L_F is the tension stiffness coefficient which depends on the ratios of both b/a and h/H. K_F and L_F increase as b/a increases or h/H increases. The stiffness and linear range of the corrugated diaphragms may be increased by the depth of the corrugations. The shape and number of corrugations have a small effect on the stiffness of the diaphragm.

Integrating the corrugated vibration diaphragm with the printed wiring board leads to the active cooling substrate device, as shown in Fig. 2. Differentiated from the vertical synthetic jet schematic presented in Fig. 1, here ACS vectors the jets by the fluidic channel to a direction tangential to the substrate. The tangential synthetic jet reduces space in the vertical direction. In addition, the footprint of the board can be reduced as well by mounting non-heat-emitting electrical components on top of the jet actuator and heat intensive units at the exit of the fluidic channels. Therefore, the ACS is embedded into the conventional PWB and adds active cooling functionality to it. The diaphragm is molded from Dyneon™ fluoroelastomer that has a tensile modulus of 1.46 MPa at 100% elongation. The diaphragm has a diameter of 33 mm. The center of the diaphragm is made from a low density material, epoxy prepreg, which is much stiffer to load the driving forces. A self-supporting air coil is mounted on the diaphragm. A permanent magnet is embedded in the PWB. As an alternating current goes through the coil, an alternating magnetic field is generated which interacts with the constant magnetic field from the permanent magnet to excite the diaphragm vibration. The cavity is a large through-hole drilled in the PWB. One fluidic channel connects the cavity to the jet exit which vectors the jet flow to the right position where hot electronic components are located. The fluidic channels can be patterned by mechanical milling or laser cutting on the prepreg laminate, then aligned and pressed to bond together. The channel height can be as small as 300 μm. Fabrication and assembly of all the ACS device components are fully compatible with the traditional PWB manufacturing process. The total thickness of the device is less than 5 mm. The driving power of the ACS device is 60 mW. The conventional air cooling techniques, i.e., fans, consume the power of 480 mW [8]. The ACS device is superior due to its easy integration with integrated circuitry and pinpoint cooling to eliminate local hot spots that may be the potential weak points of the entire circuitry.

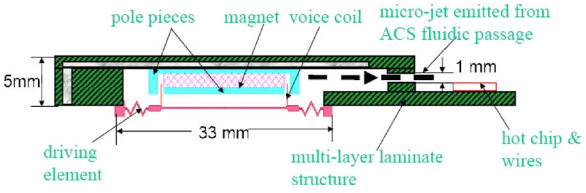

Fig. 2 Schematic of an active cooling substrate

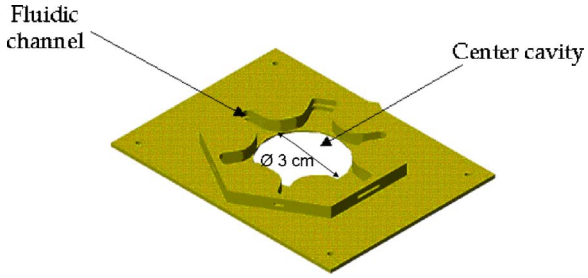

Fig. 3 Active cooling substrate testbed substrate

The dimensions of the fluidic channels have a strong impact on the linear velocity at the exit and the flow pattern development at the downstream. An active cooling substrate testbed has been designed to explore the channel width effects, as shown in Fig. 3. In simple terms, the testbed is one ACS device with six different rectangular fluidic channels connected to the center cavity. The channel dimensions are listed in Table 1. The distance from cavity center to the exit is 31 mm. The height of the channel is 1.0 mm. Variations of the channel width will change the hydraulic diameter D_h, which is defined by

$$D_h = \frac{2t_h w}{t_h + w} \tag{3}$$

where t_h is the channel height and w is the channel width. D_h can influence the exit linear velocity and the Reynolds number based on this length scale. The advantage of the testbed design is to ensure the same electromagnetic drive and the same central cavity structure are applied in each case study. Hence, the only variable is the channel dimension. When one channel is under test, the other channels are blocked by room temperature vulcanizing (RTV) silicone. Based on the prior ACS research [9–11], a coil driving current consisting of a sine wave ac current with the root mean square magnitude of 70 mA and frequency of 100 Hz is applied. To characterize the microjet cooling performance, a standard silicon based platinum heat array is used [12]. The rectangular heater array is 8 mm × 1.2 mm, which is the same heater used in the ACS cooling performance test. The heater chip functions as a heat generating component to mimic the thermal output of an integrate circuit and as a temperature sensor since the heater resistance is a direct function of temperature.

Experimental Results and Analysis

Synthetic jet fluid mechanics are investigated by particle image velocimetry (PIV) and hot-wire anemometer. PIV provides the instantaneous global view of jets development in a quantitative fashion. Hot-wire anemometer positions an electrically heated platinum wire to a specific flow-field location and measures gas velocity based on the calibrated correlation of heat convected

Table 1 Different fluidic channel dimensions

Channel Exit Number	Channel Width (mm)	Hydraulic Diameter (mm)
1	3.18	1.52
2	4.19	1.62
3	5.08	1.67
4	6.35	1.73
5	8.46	1.79
6	10.00	1.82

away from the fine wire and fluid velocity. ACS heat transfer study is facilitated by infrared thermography, which is capable to map the temperature distribution contour on the printed wiring board.

PIV determines the distance that particles have moved in the time between laser pulses. This enables the complete mapping of the velocity flow field external to the jet outlet. For instance, with the 8.46-mm-wide channel, the evolution of the synthetic jet in one vibration cycle is shown in Fig. 4. Figure 4(*a*) is a sketch showing the setup of the measurement. The testbed is placed vertically and the jet is blowing downwards. Each image is on the symmetric cut plane of the device with the *Y*-axis vertical to the outlet plane, and the *X*-axis parallel to the outlet. The channel outlet is located at (3.5 mm, 19 mm). On the left side of $x = 3.5$ mm is the board boundary on which the heater is located. Therefore, at $x \leqslant 3.5$ mm, the velocity is zero. From $0 < t/T < 0.5$ (t is the operation time, T is the period) is the impingement stroke. A counterclockwise rotating vortex is formed, rolled downward, and later breaks up. From $0.5 < t/T < 0.94$ is the intake stroke. Another clockwise rotating vortex tries to form at the outlet due to the intake air, while the primary vortex transits into turbulence and advects downstream. The velocity magnitude decreases as the distance from outlet increases.

A hot-wire anemometer is a thermal anemometer to measure fluid velocity by noting the heat convected away by the fluid. Using the same 8.46-mm-wide channel, Fig. 5 shows the centerline velocity magnitude in one vibration cycle with the measurement point of 0.80 mm away from the exit. The first half-cycle of the plot is the impingement stroke, which has a peak velocity of 8 m/s; the second half-cycle is the intake stroke, which has a peak velocity of 4 m/s. The average velocity in one cycle at this location is about 1.53 m/s. The hot-wire is also placed at another four different locations along the centerline to measure the local average velocity. The measurement points are located at 4.23, 6.35, 10.16, and 15.24 mm away from the channel exit.

PIV and hot-wire measurements are performed on the other channel designs as well. Synthetic jet flow patterns similar to demonstrated in Fig. 4 have been observed and the local average velocities have been obtained (shown in Table 2). Based on the hydraulic diameter D_h (Table 1) and the local average velocity u (Table 2), the local Reynolds number Re can be calculated by

$$\mathrm{Re} = \frac{D_h u \rho}{\mu} \tag{4}$$

where ρ is air density and μ is air viscosity at room temperature (22°C).

The cooling performance is tested in a constant temperature mode. First, the heater is ramped to a steady temperature of 100°C. The ACS jet is then turned on until the heater temperature drops to its new steady-state value of approximately 70°C. The third step of the test involves increasing the power to the heater to reach the former steady temperature of 100°C while the jet is operating.

The chip temperature is determined by the resistance measurement. The temperature distribution on the ACS is simultaneously mapped by an infrared camera. Figure 6 is the top view of the temperature contour, which is the side with the heater attached. The heater is located at 0.8 mm away from the exit using the 8.46-mm-wide channel. Similar cooling performance tests are conducted at the other exit locations, as designed in Table 2. Based on the ACS temperature distribution at two steady states when heater temperatures are at 70°C and 100°C with the operating synthetic jets, the local heat transfer coefficient at the heater location can be calculated by

$$Q = \overline{h_1} A_1 (\overline{T_1} - T_0) + \overline{h_2} A_2 (\overline{T_2} - T_0) \tag{5}$$

$$\overline{T_2} = \frac{\int T_2 dA}{A_2} \tag{6}$$

where Q is the heat dissipated from the heater array, which can be calculated by the current through the heater and the voltage across the heater. At steady states, because of energy conservation, the power input to the heater is finally dissipated from all the surfaces of the ACS device through convection. $\overline{h_1}$ is the local average heat transfer coefficient at the heater location, A_1 is the surface area of the heater, $\overline{T_1}$ is the average temperature of the heater based on the measurement of the heater resistance, T_0 is the bulk flow temperature, which is selected as the room temperature, A_2 is the ACS surface area excluding the heater area, $\overline{h_2}$ is the local average heat transfer coefficient on the area of A_2, and $\overline{T_2}$ is the average temperature of the area A_2. $\overline{T_2}$ is calculated by Eq. (6), which requires gridding the surface area into small elements and reading the individual element temperature from the thermal contour maps. The length scale on the thermal contour map can be determined by referring to the heater because the heater is the highest temperature spot on the contour and its dimensions are accurately known as 8 mm × 1.2 mm. Given two steady states, heater temperatures of 70°C and 100°C with synthetic jets, Eq. (5) can be solved to obtain $\overline{h_1}$ and $\overline{h_2}$. This method depends on the assumption that the fluid mechanics of a specific synthetic jet defines certain jet heat transfer capability (i.e., the flow pattern dominates the heat transfer phenomena and the jet heat convection is independent of the heater temperature). This assumption is valid because the heater temperature difference between the two steady states is not large enough to dramatically change the airflow physical properties (i.e., density and viscosity), and the bulk airflow reference temperature is selected as the room temperature, independent of the heater temperature. Major experimental uncertainties in the calculated heat transfer coefficient are introduced from the second term of Eq. (5), the average temperature $\overline{T_2}$, and the temperature distribution area A_2, because the accurate pixel-by-pixel temperature reading cannot be obtained from the IR camera images. $\overline{T_2}$ is estimated based on larger temperature contour segments (compared with the IR camera pixel size), which leads to some errors. The largest spatial variation occurs when the heater is placed at the closest location to the jet outlet and the heater temperature is raised up to 100°C because there is a sharp temperature gradient in a relatively small area. Systematic uncertainty contributed from $\overline{T_2}$ at this worst scenario is ±10°C and uncertainty from A_2 is ±10 mm^2. These errors propagate through the data reduction equations (5) and (6) and yield a systematic error of 14 W/m^2 K. The random error is estimated at less than 2 W/m^2 K. The overall uncertainty at the location closest to the jet exit is ±15 W/m^2 K. At the locations further away from the jet exit, the spatial variation is relatively smaller and thus the systematic uncertainty decreases. The uncertainties at the locations of 4.23, 6.35, 10.16, and 15.24 mm away from the jet exit are 13, 12, 10, and 8 W/m^2 K, respectively.

The calculated local heat transfer coefficients are plotted in Fig. 7. Observation of Fig. 7 indicates the local heat transfer coefficients have two local maxima. The first maximum is the position near the exit, which is the primary optimal cooling location. The high heat transfer coefficient is caused by the high linear velocity at the exit. The second maximum is the position where 6–10 mm away from the exit, which is the secondary optimal cooling location. It is believed that the secondary optimal position is where the vortex is fully developed and transits to turbulent flow. The higher turbulence contributes to the local heat transfer. The secondary optimal location can be related to a characteristic length scale L_0, which is related to stroke length and is defined by

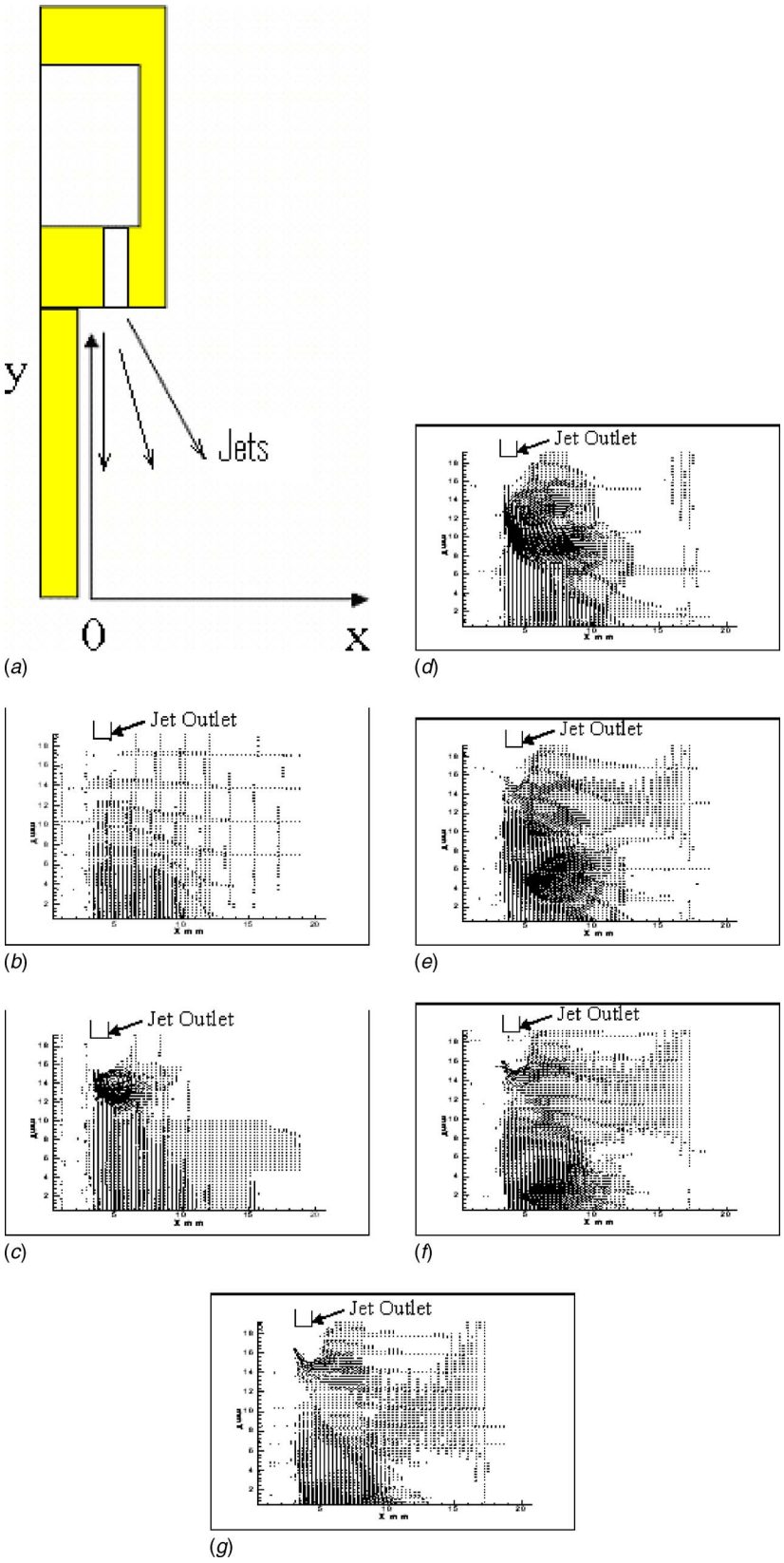

Fig. 4 Evolution of a synthetic jet (a) PIV measurement setup. (b) PIV image at $t/T=0$ (c) PIV image at $t/T=0.17$ (d) PIV image at $t/T=0.33$. (e) PIV image at $t/T=0.50$ (f) PIV image at $t/T=0.66$ (g) PIV image at $t/T=0.83$.

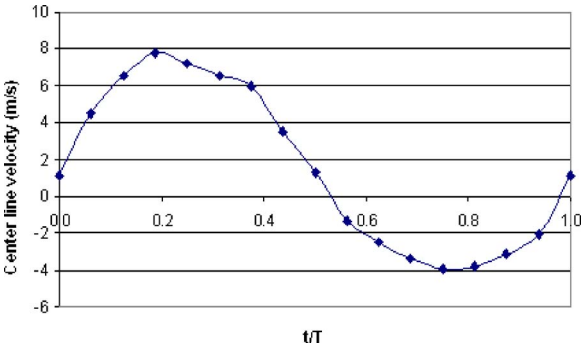

Fig. 5 Centerline velocity for 8.46-mm-wide channel at 0.8 mm away from exit

$$L_0 = \int_0^{T/2} u_0(t)dt \tag{7}$$

where $u_0(t)$ is the instantaneous velocity at the exit on the impingement stroke, which is approximated by the velocity measured at the location of 0.8 mm away from exit by hot-wire. The calculated L_0 values for different channels are listed in Table 3. In addition, from Fig. 7, the optimal channel width can be obtained at about 4.19 mm, which has the best cooling performance. When the orifice dimension is small (i.e., $b \leqslant 3.18$ mm), the flow viscous effects become important. The effective flow area is smaller than the actual channel exit area. Therefore, the volumetric flow rate is reduced. When the orifice dimension is large (i.e., $b \geqslant 5.08$ mm), the viscous effects diminish. Mass conservation requires that the flow velocity should decrease proportionally to the orifice area. Therefore, there is an optimal fluidic channel dimension for a given actuator design.

Since the local heat transfer coefficient is known, the local average Nusselt number can be calculated by

$$\overline{\mathrm{Nu}} = \frac{\overline{h_1} D_h}{k} \tag{8}$$

where k is heat conductivity. For engineering applications, an empirical correlation of heat transfer (Nu) and fluid mechanics (Re) can be derived by dimensionless group analysis. Normally for forced convection, the Nusselt number (Nu) is a function of the Reynolds number (Re), the Prandlt number (Pr) and some dimension groups (i.e., D_h/L_0, L_x/L_0) as

$$\mathrm{Nu} = f(\mathrm{Re}, \mathrm{Pr}, D_h/L_0, L_x/L_0) \tag{9}$$

$$\mathrm{Pr} = \frac{C_p \mu}{k} \tag{10}$$

where C_p is air heat capacity and L_x is the distance from the heater to the jet exit. Since the airflow reference temperature is selected to be the constant room temperature, Pr is constant (0.70) in all the cases and is dropped off from Eq. (9). Hence, Nu is simplified as the function of Re, D_h/L_0 and L_x/L_0.

In this research, the simplest power law function is applied to curve fit the correlation of Nu and Re, D_h/L_0, L_x/L_0. The data from different channels are employed to fit the function. The analytical equation is derived as

Table 2 Average centerline velocities (m/s) at different exit locations

Fluid Channel	0.80 mm from Channel Exit	4.23 mm from Channel Exit	6.35 mm from Channel Exit	10.16 mm from Channel Exit	15.24 mm from Channel Exit
1	3.02	3.22	2.94	2.29	1.72
2	2.71	2.59	2.2	1.71	1.15
3	1.47	1.69	1.24	0.92	0.61
4	1.77	1.13	0.80	0.58	0.39
5	1.53	1.10	0.80	0.68	0.67
6	1.19	1.09	0.98	0.46	0.38

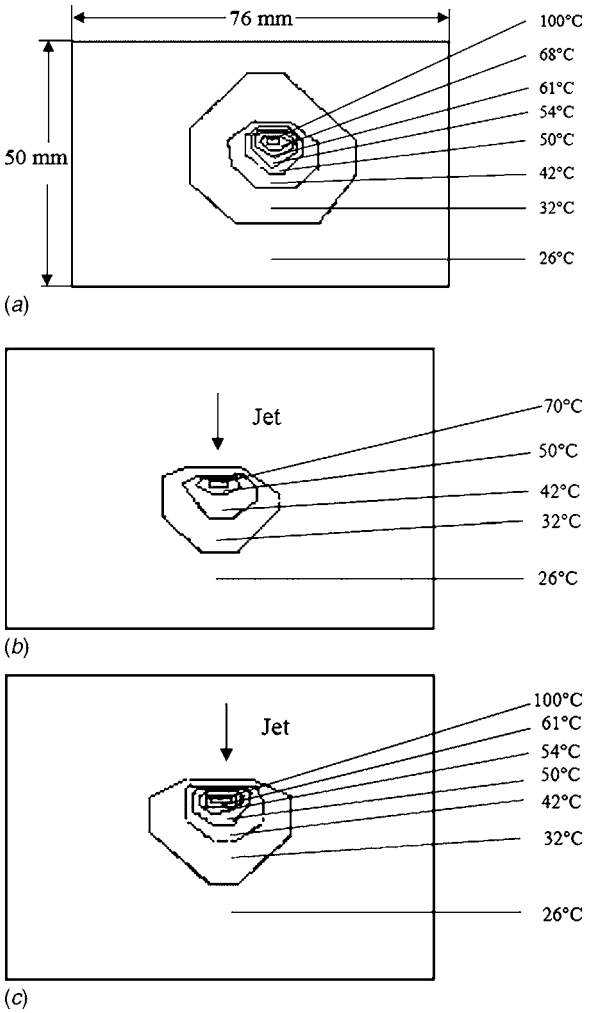

Fig. 6 Temperature contour on PWB substrate in one cooling test cycle (a) without jet, heater at 100°C, (b) with jet, heater at 70°C (c), and with jet, heater at 100°C

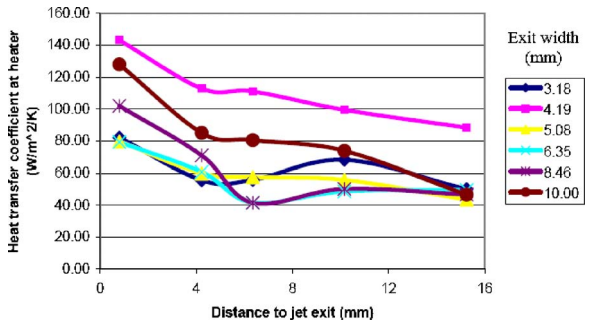

Fig. 7 Local heat transfer coefficient along the jet centerline

Table 3 Stroke lengths for different fluidic channels

Channel exit	1	2	3	4	5	6
Stroke Length (mm)	24.0	22.2	14.7	17.4	13.9	13.4

$$\overline{\mathrm{Nu}} = 3.1533\mathrm{Re}^{0.1901}\left(\frac{D_h}{L_0}\right)^{0.3321}\left(\frac{L_x}{L_0}\right)^{-0.1501} \tag{11}$$

Equation (11) is applicable to Re from 7000 to 70,000, D_h/L_0 from 0.06 to 0.14 and L_x/L_0 from 0.03 to 1.40. The overall error of the curve fitting equation is less than 24% when compared with all the data obtained at different channel dimensions (shown in Table 4). Therefore, the correlation equation (11) is acceptable to demonstrate the relationship between the synthetic jets fluid mechanics and the heat transfer, and is capable to approximate the cooling performance of certain synthetic jets.

A magnitude analysis can be performed on Eq. (11) to extract the dimensional impacts on the synthetic jet heat removal and to determine the optimal dimensions for best cooling performance. In the following text, the variables in [ ] denote the magnitudes of the variables. Based on the definitions of Nu and Re, $[\overline{\mathrm{Nu}}]$ is proportional to the local heat transfer coefficient at the heater $[\overline{h_1}]$ and D_h, [Re] is proportional to u (average velocity over one vibration cycle) and D_h. u can have the same magnitude as u_{im}, which is the average velocity over the impingement stroke, if u_{in}, the average velocity over the intake stroke, is small and can therefore be neglected. This assumption is not valid near the jet exit. $[L_0]$ is proportional to u_{im}/f according to its definition, where f is the ac driving circuit frequency. Combining the expressions for $[\overline{\mathrm{Nu}}]$, [Re], and $[L_0]$ into Equation (11), $[\overline{h_1}]$ can be determined by

$$[\overline{h_1}] = \frac{u_{\mathrm{im}}^{0.00802} f^{0.1820}}{D_h^{0.4778} L_x^{0.1501}} \tag{12}$$

Based on mass conservation, u_{im} can be simplified as $Q_v/(t_h w)$. The volumetric flow rate Q_v can be calculated by Eq. (1). D_h is defined in Eq. (3). Therefore, Eq. (12) can be expressed as

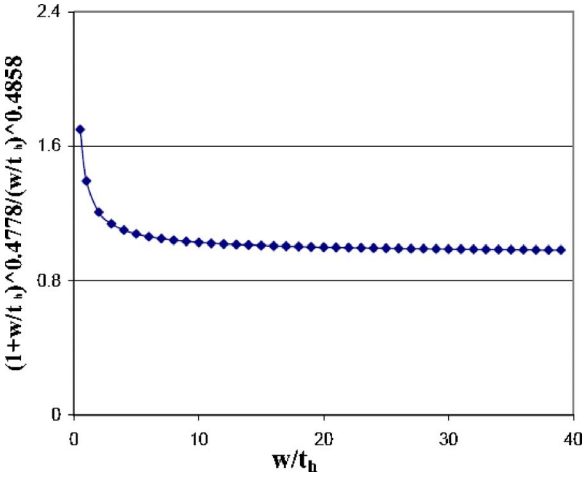

Fig. 8 The fluidic channel width impacts on heat transfer

$$[\overline{h_1}] = [(a^2 + ab + b^2)^{0.00802} D^{0.00802} f^{0.1900}]\left\{\frac{1}{L_x^{0.1501}}\right\} \times \left[\frac{\left(1 + \frac{w}{t_h}\right)^{0.4778}}{t_h^{0.4938}\left(\frac{w}{t_h}\right)^{0.4858}}\right] \tag{13}$$

Equation (13) is split into three groups (as indicated by the brackets). The first group includes the parameters related to the diaphragm design (i.e., the diaphragm radius a, the diaphragm rigid center radius b, the diaphragm deflection D, and the excitation frequency f). The excitation frequency has a stronger influence on improving the cooling performance than do the diaphragm dimensions and deflection. The diaphragm dimensions, frequency, and deflection are all related through Eq. (2), which is the criterion for minimizing the driving force. It is necessary to design the diaphragm such that the terms within the first bracket of Eq. (13) are maximized and the driving force (Eq. (2)) is minimized. In addition, there are some constraints from practical ap-

Table 4 Nusselt number experimental results and curve fitting results

Fluid Channel		1	2	3	4	5	6
0.80 mm from Channel Exit	Experiment	4.80	8.88	5.12	5.27	7.01	8.94
	Curve fitting	6.17	6.32	6.18	6.32	6.52	6.31
4.23 mm from Channel Exit	Experiment	3.25	7.00	3.85	4.03	4.88	5.94
	Curve fitting	4.86	4.88	4.94	4.51	4.76	4.83
6.35 mm from Channel Exit	Experiment	3.26	6.89	3.69	2.76	2.85	5.62
	Curve fitting	4.49	4.45	4.38	3.98	4.22	4.45
10.16 mm from Channel Exit	Experiment	3.99	6.18	3.58	3.22	3.45	5.15
	Curve fitting	3.99	3.95	3.86	3.48	3.81	3.59
15,24 mm from Channel Exit	Experiment	2.92	5.48	2.79	3.29	3.21	3.25
	Curve fitting	3.56	3.45	3.35	3.04	3.57	3.26

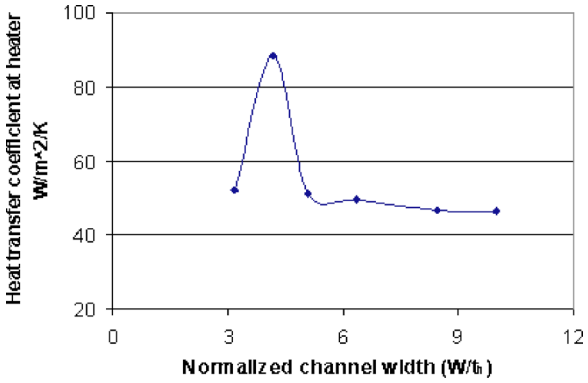

Fig. 9 Heat transfer coefficient vs normalized channel width at 15.24 mm away from the jet exit

plications. The excitation frequency can not be too high, which could induce loud noise and reduce the diaphragm deflection dramatically. Thus, the resonance frequency of the system, i.e., 100 Hz, is applied for diaphragm excitation. With the real estate concerns on the PWB, the diaphragm can not be too large that it occupies vast footprint, and hence limits the device density on the board. The diaphragm radius a is selected as the largest possible size on the board to maximize the jet cooling capacity, such as 1.5 cm in this study. The diaphragm rigid center radius and the corrugation structures are determined from Eq. (2) to maximize the diaphragm deflection.

The second group shows that $\overline{h_1}$ is inversely proportional to the distance between the heater and the jet outlet. The model indicates that it is better to place the heat generating components close to the jet exit. Due to the simplicity of the empirical equation (11), it cannot capture the fine details of the synthetic jet fluid mechanics; for example, the secondary local cooling maxim. Based on Figs. 4 and 7, within $0.5L_0$ is the range in which the jet has good cooling performance whereby the jet vortices entrain the surrounding air and develop into turbulent flow.

The third group is related to the fluidic channel dimensions (i.e., the channel height t_h and width w). The channel height t_h is normally small due to the low profile design requirement. t_h is assumed to be a constant and factored out in Eq. (13). Figure 8 is the plot of function $(1+w/t_h)^{0.4778}/(w/t_h)^{0.48582}$ versus the ratio of w/t_h. The figure and Eq. (13) indicate that heat transfer becomes weaker as the fluidic channel width increases. However, if the channel width is too small, the jet flow rate would be reduced due to the strong viscous effects. Figure 9 shows the local heat transfer coefficients which are calculated based on Eq. (5) for different channel widths at 15.24 mm away from the jet exit. In these measurements, the channel height, the diaphragm dimensions, the driving current magnitude and frequency are the same. Figure 9 indicates a regime for the optimal channel width is between $3t_h$ and $5t_h$ where $\overline{h_1}$ can obtain a high value and the viscous effects are minimal.

In summary, the magnitude analysis provides guidelines for the ACS design. Combined with some other application constraints, the optimal designs can be determined, such as, the diaphragm radius is the largest possible size on board; the excitation frequency is the system resonance frequency; the optimal cooling location is within $0.5\ L_0$; and the optimal fluidic channel width is between $3t_h$ and $5t_h$. The empirical equations (2) and (11) offer the analytical solution to design an active cooling substrate device. Equation (2) determines the correlation between the synthetic jet generation device and its fluid mechanics, which confines the actuator diaphragm design, and Eq. (11) is the correlation between synthetic jet fluid mechanics and heat transfer which provides guidance to optimize the fluidic channel and cooling location. Therefore, with a known dimension ACS device, its cooling performance can be predicted; also, with a certain thermal management requirement, the desired cooling device ACS dimensions can be derived.

Conclusions

In this research, the microfluidic channel dimensional impact on ACS microjet fluid mechanics and heat transfer have been explored. The optimal channel dimensions and the optimal cooling location have been obtained. The derived correlation equation can be applied in future thermal management design which predicts the relationship between forced heat convection and the fluid mechanics for synthetic jets. In addition, this research provides analytical methodologies to optimize the synthetic jets based cooling devices, active cooling substrates, with concerns of cooling performance, power consumption and real estate issues.

References

[1] Gelsinger, P., 2001, "Microprocessors for the Millennium: Challenges, Opportunities, and New Frontiers," *Proceedings of 2001 IEEE International Solid-State Circuits Conference*, p. 22.
[2] Tummala, R., 2001, *Fundamentals of Microsystems Packaging*, McGraw-Hill, New York.
[3] Jacobs, J., James, R., Ratcliff, C., and Glezer, A., 1993, "Turbulent Jets Induced by Surface Actuators," AIAA Shear Flow Conference, AIAA 93–3243.
[4] Smith, B., and Glezer, A., 1998, "The Formation and Evolution of Synthetic Jets," Phys. Fluids, **10**(9), p. 2281.
[5] Rathnasingham, R., and Breuer, K., 1997, "Coupled Fluid-Structure Characteristics of Actuators for Flow Control," AIAA J., **35**(5), p. 382.
[6] Rediniotis, O., Ko, J., Yue, X., and Kurdila, A., 1999, "Synthetic Jets, Their Reduced Order Modeling and Applications to Flow Control," 37th Aerospace Sciences Meeting & Exhibit, AIAA99–1000.
[7] Giovanni, M. D., 1982, *Flat and Corrugated Diaphragm Design Handbook*, Marcel Dekker Inc., New York.
[8] Kim, S., and Lee, S., 1996, *Air Cooling Technology for Electronic Equipment*, CRC Press, Boca Raton, FL.
[9] Wang, Y., Bidstrup, S., Yuan, G., and Allen, M., 2002, "Printed-Wiring-Board Microfluidics for Thermal Management of Electronic Systems," *Proceedings of 2002 ECS International Symposium*, May, pp. 161–170.
[10] Wang, Y., Yuan, G., Yoon, Y., Allen, M., and Bidstrup, S., 2003, "A MEMS Active Cooling Substrate for Microelectronics Thermal Management," *Proceedings of 2003 ASME International Mechanical Engineering Congress and R&D Exposition*, Nov., IMECE2003–42799.
[11] Wang, Y., Yuan, G., Yoon, Y., Allen, M., and Bidstrup, S., 2005, "Active Cooling Substrates for Thermal Management of Microelectronics," IEEE Trans. Compon. Packag. Technol., **28**(3), p. 477.
[12] Yoon, Y. K., and Allen, M. G., 2001, "Pt Heater/Sensor Microarray for Distributed Fluidic Cooling Assessment," *Proceedings of 2001 ASME IMECE/MEMS-23894*.